Research Square

Preprints are preliminary reports that have not undergone peer review.
They should not be considered conclusive, used to inform clinical practice,
or referenced by the media as validated information.

Decoding the multiregional atlas of Parkinson's disease at single-cell resolution

Juan Andrés Tejedor-Serrano
Universitat Politècnica de València https://orcid.org/0009-0002-9722-7545
Ángeles Arzalluz-Luque
Spanish National Research Council https://orcid.org/0000-0002-2959-0134
Sonia Tarazona
sotacam@eio.upv.es

Universitat Politècnica de València https://orcid.org/0000-0001-5346-1407
Jordi Martorell-Marugán
jordi.martorell@fisabio.es

Foundation for the Promotion of Health and Biomedical Research in the Valencian Region (FISABIO)
https://orcid.org/0000-0002-5186-0735

Research Article

Keywords: Parkinson's disease, snRNA-Seq, brain atlas, computational neuroscience

Posted Date: June 11th, 2026

DOI: https://doi.org/10.21203/rs.3.rs-9220144/v2

License: This work is licensed under a Creative Commons Attribution 4.0 International License.
Read Full License

Additional Declarations:
The authors declare no competing interests.

This study is based exclusively on previously collected and de-identified human data obtained through the Accelerating Medicines Partnership Parkinson's Disease (AMP-PD) consortium. The data used in this work were generated from samples collected by four independent biobanks under their respective institutional review board (IRB) or ethics committee approvals, with informed consent obtained from all participants at the time of sample collection.We did not generate primary data, did not have access to identifiable participant information, and performed only secondary analyses of existing, de-identified

datasets made available by AMP-PD in accordance with its data access policies. Therefore, we consider than no additional IRB or ethics committee approval was required for this secondary data analysis.

Decoding the multiregional atlas of Parkinson's disease at single-cell resolution

Juan Andrés Tejedor-Serrano[1], Ángeles Arzalluz-Luque[2], Sonia Tarazona[1,*], and Jordi Martorell-Marugán[3,*]

[1]Department of Applied Statistics and Operational Research and Quality, Universitat Politècnica de València, Camino de Vera s/n, 46022 Valencia, Spain

[2]Instituto de Neurociencias (CSIC-UMH), Avenida Doctor Santiago Ramón y Cajal s/n, 03550 Alicante, Spain

[3]Computational Neuroscience. Joint Unit in Biomedical Imaging and Artificial Intelligence FISABIO-CIPF. Foundation for the Promotion of Health and Biomedical Research in the Valencian Region (Fisabio), 46012, Valencia, Spain

[*]Corresponding authors: jordi.martorell@fisabio.es; sotacam@eio.upv.es

Abstract

Characterizing the multiregional cellular landscape of Parkinson's disease (PD) is essential for understanding its broad impact beyond the midbrain. To advance that goal, we analyzed single-nucleus RNA sequencing data from over 2.2 million nuclei across five brain regions from 93 donors. We identified region-specific alterations in cell population abundances, including a reduction in layer 2/3 excitatory neurons in the primary motor cortex and an expansion of specific astrocyte, microglial and oligodendrocyte precursor subtypes in the dorsal motor nucleus of the vagus nerve (DMNX). We found that, while most transcriptional changes are cell-type-specific, a core set of markers, including *BNIP3L*, *WSB1* and the non-coding RNA *LINC00862*, are ubiquitously dysregulated across lineages. Furthermore, glial and vascular populations in the DMNX exhibit convergent transcriptional profiles characterized by mitochondrial dysfunction, neuroinflammation and extracellular matrix remodeling. These results provide a high-resolution characterization of molecular and cellular changes in PD, demonstrating that disease-associated alterations are highly dependent on the intersection of cell identity and anatomical location.

Introduction

Parkinson's disease (PD) is a neurodegenerative disorder characterized by alpha-synuclein (α-syn) aggregation into Lewy bodies (LBs) and dopaminergic neuron loss in the substantia nigra pars compacta (SN)[1;2]. According to the Braak staging hypothesis, α-syn pathology propagates along a defined spatiotemporal axis, initiating in the lower brainstem before ascending to the midbrain and eventually reaching the neocortex[3].

Despite this multi-region nature, molecular profiling efforts—including recent single-nucleus RNA sequencing (snRNA-seq) studies—have focused primarily on SN and the selective vulnerability of dopaminergic neurons[4;5], offering limited insight into how neuronal populations beyond the SN degenerate or how glial cells respond across brain areas[6–8]. A brain-wide, cell-type-resolved understanding of PD pathology is therefore lacking.

To address this gap, consortia such as the Accelerating Medicines Partnership in Parkinson's Disease (AMP-PD) have undertaken large-scale molecular profiling of individual cell types across multiple brain regions using single-nucleus RNA sequencing (snRNA-seq)[9]. However, the high dimensionality, sparse nature and complex experimental design inherent to single-cell data pose substantial challenges for extracting biologically meaningful insights. Addressing these challenges, we analyzed the multi-region snRNA-seq data generated by AMP-PD to present a comprehensive atlas of the human brain in PD, comprising over 2.2 million high-quality nuclei from 93 donors. Sampled tissue covered five brain regions along the LB pathology progression axis: the dorsal motor nucleus of the vagus nerve (DMNX), globus pallidus interna (GPI), primary motor cortex (PMC), dorsolateral prefrontal cortex (PFC) and primary visual cortex (PVC). By characterizing neuronal and glial populations and their subtypes across these regions, we identify region and subtype-specific compositional and transcriptomic alterations, providing a granular resource for understanding the key molecular changes underlying PD. To facilitate community access, we provide an interactive web application (`https://juantejedor-pd-atlas-explorer.share.connect.posit.cloud/`) for visualization of cell-type- and region-specific alterations.

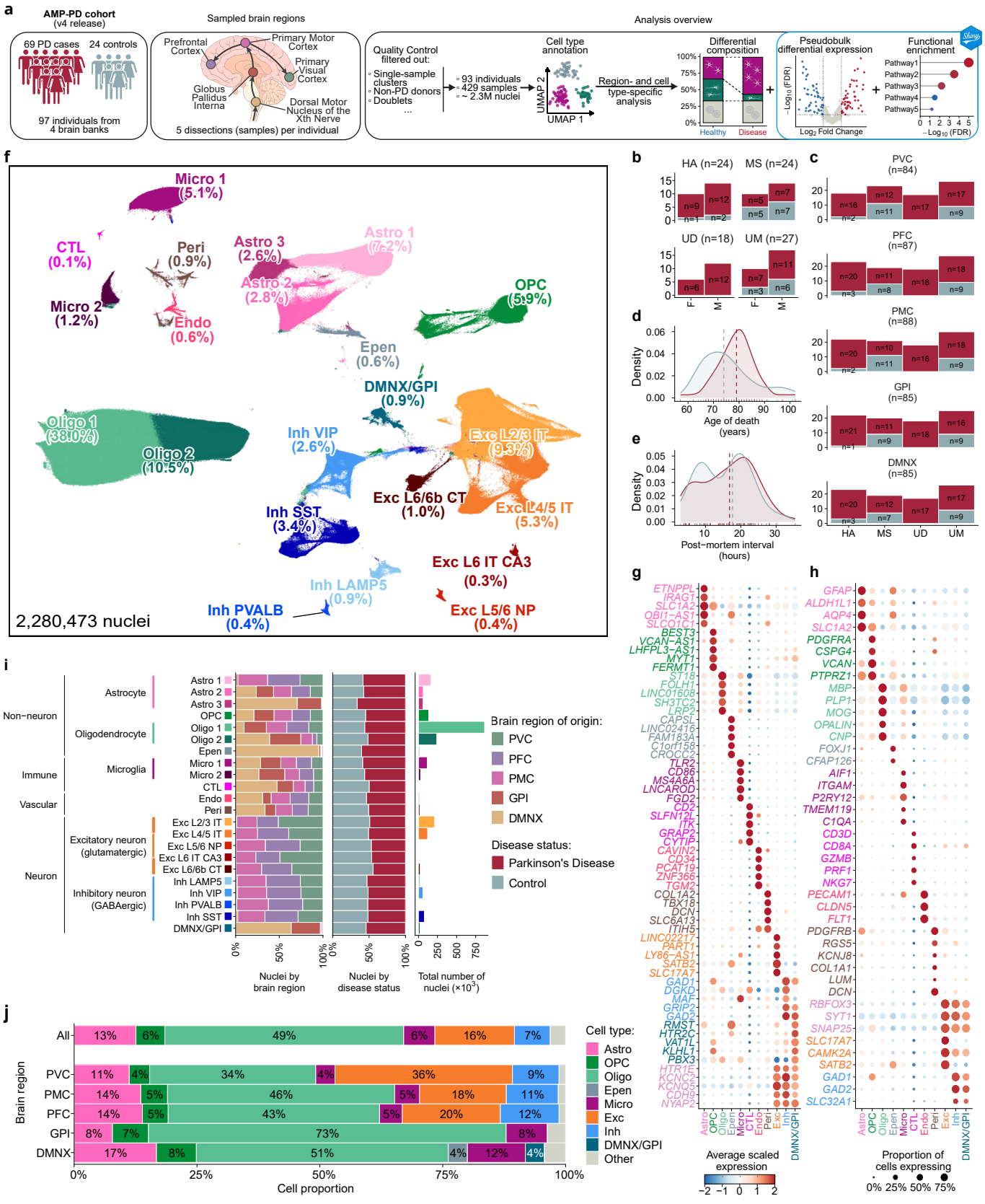


Figure 1: Single-nucleus RNA sequencing of the AMP-PD Parkinson's disease cohort across five brain regions.
a Overview of the AMP-PD snRNA-seq study design and analytical workflow. Brain tissue from 93 donors was profiled across five brain regions, including regions affected early in Parkinson's disease (DMNX and GPI) and cortical regions affected later (PMC, PFC and PVC). **b** Distribution of donors across key covariates stratified by disease status, including brain bank of origin and sex. HA, NIH NeuroBiobank at the Harvard Brain Tissue Resource Center; MS, Mount Sinai Brain Bank; UD, University of Miami Udall Center of Excellence for Parkinson's Disease Research; UM, University of Miami Brain Endowment Bank; M, male; F, female. **c** Number of samples (dissections) per brain region stratified by disease status and brain bank. **d**–**e** Distribution of age at death (**d**) and post-mortem interval (**e**) across donors, stratified by disease status. Dashed lines indicate medians. **f** UMAP embedding of nuclei colored by annotated cell subtype. Related major cell types share color hues. **g**–**h** Dot plots of data-driven (**g**) and literature-curated (**h**) marker genes used for cell type annotation. Data-driven markers correspond to the top five genes per cell type from one-vs-rest pseudobulk differential expression analysis. Dot size represents the proportion of cells within a given cell type expressing the gene; color indicates mean scaled pseudobulk expression (z-scored per gene across cell types). Gene labels are colored by cell type. Neuronal populations include additional pan-neuronal markers (light pink). **i** Hierarchical organization of cell populations into supertypes, types and subtypes, with relative abundances across brain regions, disease status and total nuclei counts. Disease-stratified abundances represent the mean number of nuclei per donor. **j** Regional composition of cell types across all samples ('All') and within each brain region. Cell types <4% were grouped as 'Other'. Percentages displayed within bars indicate relative cell type abundances.

Results

Cellular landscape of the AMP-PD multi-region snRNA-seq cohort

To construct a comprehensive cellular atlas of PD and provide a robust foundation for dissecting cell-type- and region-specific disease alterations, we analyzed the extensive multi-region snRNA-seq dataset provided by the AMP-PD consortium (Fig. 1a). After quality control, integration and annotation we retained 2,280,473 high-quality nuclei from 429 post-mortem samples across 93 individuals (Fig. 1a; Supplementary Fig. 1a), spanning early-affected subcortical regions—DMNX (15.1% of nuclei) and GPI (18.6%)—to susceptible neocortical regions including the PMC (23.6%), PFC (22.1%) and PVC (20.8%).

The final cohort included 69 PD donors and 24 controls without a neurodegenerative disease diagnosis, resulting in a ∼3:1 PD-to-control ratio. This ratio was balanced across sexes (Fisher's exact test, $p = 1$; Fig. 1b) and brain regions ($p = 0.97$; Fig. 1c), but unbalanced across brain banks, with one bank providing samples exclusively from PD donors ($p < 0.001$; Fig. 1b). PD donors were modestly older than controls (median [IQR]: 79 [8] vs. 74 [13] years; Wilcoxon rank-sum test, $p = 0.026$; Fig. 1d), whereas post-mortem interval (PMI) did not differ significantly between groups (16.8 [11.7] vs. 17.6 [11.0] hours; $p = 0.556$; Fig. 1e).

Data integration effectively mitigated the influence of technical and donor-specific covariates on cell clustering. No clusters were driven by sequencing batch, brain bank, donor identity or PMI (Supplementary Fig. 1b-e). While clusters did not segregate by disease status (Supplementary Fig. 1f), implying shared broad cell identities between PD and controls, pronounced regional segregation confirmed the retention of anatomical specificity (Supplementary Fig. 1g).

We identified 22 cell types, grouped into 11 main cellular classes (Fig. 1f–j). Neuronal populations comprised five excitatory subtypes (Exc L2/3 IT, L4/5 IT, L5/6 NP, L6 IT CA3 and L6/6b CT), defined by cortical layer location and projection type, and four inhibitory subtypes (e.g., Inh LAMP5, VIP, PVALB and SST) classified based on canonical interneuron marker genes. In addition, we identified a subcortical neuron population restricted to the DMNX and GPI, hereafter referred to as DMNX/GPI neurons. Vascular cells included endothelial cells (Endo) and pericytes (Peri), while immune populations comprised two microglial states (Micro) and cytotoxic T lymphocytes (CTL). Glial populations included three astrocyte subtypes (Astro), two oligodendrocyte subtypes (Oligo), oligodendrocyte precursor cells (OPC) and ependymal cells (Epen).

Oligodendrocytes were the most abundant cell type, accounting for 48.5% of all nuclei and up

to 73% of GPI nuclei (Fig. 1f,j). This predominance aligns with previous single-nuclei atlases of the human brain[5;10] and reflects the high glia-to-neuron ratio described in GPI[11]. Marked regional differences in cellular composition were observed (Fig. 1i,j): excitatory and inhibitory neurons were largely restricted to neocortical regions (PFC, PMC, PVC), the DMNX/GPI neuronal subtype to subcortical regions, and ependymal cells exclusively to the DMNX. Within cell types, Astro 1 was primarily cortical and Astro 3 more prevalent in non-cortical regions.

Annotated cell types displayed robust expression of canonical marker genes[12–15] (Fig. 1g): *RBFOX3* (neurons), *SLC17A7* (Exc), *GAD1* and *GAD2* (Inh), *GFAP* (Astro), *PDGFRA* (OPC), *MBP* (Oligo), *FOXJ1* (Epen), *ITGAM* (Micro), *CD8A* (CTL), *PECAM1* (Endo) and *PDGFRB* (Peri), validating the atlas annotations. Pseudobulk differential expression across clusters (see Methods) identified highly specific data-driven markers (Fig. 1h), a substantial fraction of which were long non-coding RNAs (lncRNAs), including *RMST* and *PART1*, antisense RNAs such as *VCAN-AS1* (OPC; more specific than canonical marker *VCAN*) and *LY86-AS1* (Exc), and previously uncharacterized transcripts—*LINC02217* (Exc), *LINC02416* (Epen) and *LINC01608* (Oligo)—also showing high cell type specificity, suggesting their potential as novel nuclear marker genes. These findings confirm that lncRNAs represent a relevant and underexplored class of markers in snRNA-seq, consistent with previous human brain studies[13;16–18].

Parkinson's Disease drives glial expansion and oligodendrocyte loss in subcortical regions

To determine how PD affects cellular composition across brain regions, we modeled changes in cell type relative abundance using tascCODA[19;20], a Bayesian compositional method that accounts for data compositionality, cell type lineage hierarchies and sample-level covariates (see Methods). Following Gabitto et al.[21], cell types with a credible decrease in abundance in PD were classified as *PD-vulnerable*, those with a credible increase as *PD-associated*, and those with no credible change as *unaffected*.

Overall, most cell types remained unaffected across brain regions; only a limited number, and only in specific regions, exhibited credible changes in abundance (Fig. 2a–d; Supplementary Fig. 2a–e). Credible associations with covariates such as sex and age at death were also identified (Supplementary Fig. 3) and all effects remained highly consistent regardless of the reference cell type used (Supplementary Fig. 4).

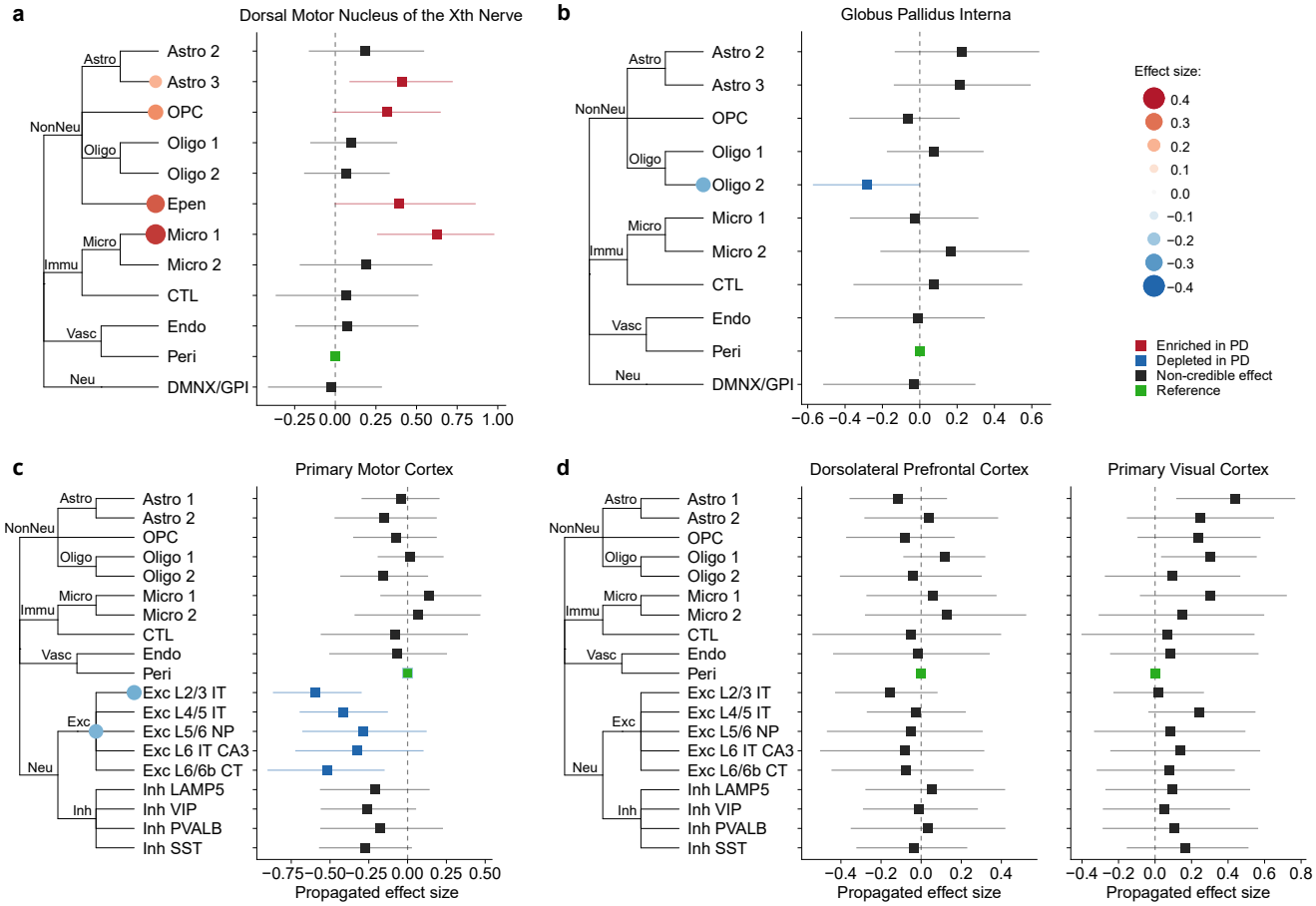


Figure 2: Changes in cell type composition across brain regions in Parkinson's disease.
a–d Cell type hierarchies underlying compositional changes across brain regions in Parkinson's disease. Shown are tascCODA model estimates of node-level and propagated feature-level effects (see Methods and Supplementary Note 1) associated with PD for each brain region, including regions with credible compositional changes—DMNX (**a**), GPI (**b**) and PMC (**c**)—and regions without credible changes—PFC (**d**, left) and PVC (**d**, right). In each panel, the cell type hierarchy is displayed as a dendrogram (left side of each panel); a colored dot at a node indicates a credible change in relative abundance at that node, with dot color reflecting the direction of the node-level effect (red, enriched in PD; blue, depleted in PD) and dot size reflecting effect magnitude. The forest plots (right side of each panel) show propagated effect sizes for each cell subtype. Squares represent posterior mean estimates and error bars denote 95% credible intervals (CI). Square color indicates whether the propagated effect is credibly increased (red), credibly decreased (blue), or non-credible (dark gray) in PD relative to controls. The pericyte cell type, used as the reference, is highlighted in green.

The most pronounced compositional perturbations were observed in the DMNX, a region known for early pathological involvement in PD[3]. Four cell subtypes were PD-associated: Astro 3, OPCs, ependymal cells and Micro 1, with model-estimated increases of 11%, 18%, 26% and 31%, respectively (see Methods for details; Fig. 2a; Supplementary Fig. 2a). The observed proliferation of microglia and astrocytes aligns with recent snRNA-seq studies reporting 'pan-glial' activation in the SN of PD patients[6;22]. Similarly, OPC proliferation in PD has also been documented in the SN[23]. Our findings extend these results to the DMNX, a region affected earlier than the SN according to Braak staging, likely reflecting an initial response to pronounced α-syn accumulation and the associated cellular stress. Notably, the selective expansion of specific microglial and astrocyte subtypes, while others within the same lineage remain stable, implies specialized functional roles for these populations within the DMNX. Lastly, although ependymal cells are implicated in PD pathology through α-syn internalization and accumulation[24], evidence for their proliferative expansion remains limited; however, animal models indicate that quiescent ependymal cells can be activated by local injury to divide and self-renew[25], providing a plausible mechanism for the expansion observed here.

In the GPI, compositional shifts were similarly limited to glial populations. The Oligo 2 subtype was selectively vulnerable, exhibiting a credible 17% reduction in relative abundance in PD donors compared to controls (Fig. 2b; Supplementary Fig. 2b), while the Oligo 1 population remained unchanged. Oligodendrocyte depletion is a consistent finding in PD, with prior snRNA-seq studies reporting significant losses in the midbrain[6], including the SN[22], as well as in the putamen[26]. Our results extend this pattern of vulnerability to the GPI—a key output nucleus of the basal ganglia—indicating that oligodendrocyte loss is not restricted to midbrain structures but also involves downstream motor circuit regions. This is further supported by reports of oligodendrocyte loss in the GPI in multiple system atrophy (MSA)[27]—a synucleinopathy that shares core motor features with PD—and recent synthetic MRI evidence of reduced myelin content in the GPI of PD patients[28]. The selective depletion of Oligo 2 provides a plausible cellular basis for this demyelination—given the role of oligodendrocytes in myelin synthesis and maintenance—in a region characterized by dense, highly myelinated white matter[29]. Moreover, a MPTP-lesioned macaque model of PD showed depletion of hydroxylated sulfatides—lipids essential for myelin stability—in the GPI[30]. These findings suggest that Oligo 2 loss may impair myelin-associated lipid homeostasis, potentially contributing to white matter degeneration and basal ganglia motor circuit dysfunction in PD.

Selective depletion of excitatory neurons in the primary motor cortex drives regional vulnerability in Parkinson's Disease

Regarding cortical regions, the PMC exhibited specific neuronal vulnerabilities. While inhibitory neurons and glial populations remained unaffected, several excitatory subtypes were identified as PD-vulnerable, exhibiting marked depletion relative to controls: Exc L2/3 IT (estimated 33% reduction), Exc L4/5 IT, Exc L5/6 NP, Exc L6 IT CA3 and Exc L6/6b CT (all showing an estimated 14% reduction) (Fig. 2c; Supplementary Fig. 2c). The hierarchy-aware model identified this vulnerability as a shared feature of the excitatory lineage, with upper-layer IT neurons showing the most pronounced depletion (Fig. 2c). This specific loss of cortical excitatory populations contrasts with the stability observed in inhibitory neurons, for which no credible changes were detected, consistent with previous reports of preserved cortical interneurons in PD[31]. To our knowledge, depletion of excitatory neurons in the PMC has not been previously reported in PD.

While altered neuronal activity and excitability in the PMC are well-documented in PD[32;33] and thought to contribute to motor symptoms, evidence for structural loss of specific subtypes in this region has been lacking. Previous neuropathological studies localized neuronal degeneration primarily to the pre-supplementary motor area (pre-SMA) and suggested the PMC does not exhibit significant neuronal loss[31;34;35]—a finding this atlas challenges, likely enabled by the higher resolution of transcriptomic subtyping. However, the mechanisms underlying this selective vulnerability remain unclear. According to Braak staging, neocortical regions such as the PMC are typically affected only in advanced stages of PD[36]. Although several studies have reported the presence of LBs in this region, α-syn inclusions are less abundant in the PMC than in adjacent motor areas and accumulate preferentially in deep-layer (L5/6) neurons, while upper layers (L2/3) generally show fewer inclusions[35;37;38]. The pronounced L2/3 IT depletion therefore suggests mechanisms beyond direct LB pathology. One possibility is axonal 'dying-back' degeneration: deep-layer neuron dysfunction could lead to degeneration of their presynaptic partners located in upper layers through disruption of trophic support[39]. Consistent with this, studies in PD mouse models have shown that dopaminergic depletion in the SN can alter the excitability and functional properties of deep-layer neurons in the PMC[33;40]. Under this scenario, early functional impairment of deep-layer neurons—together with their higher propensity to accumulate LBs—could contribute to the degeneration of this population and subsequently affect their upstream presynaptic partners, including L2/3 neurons, which may progressively lose trophic support and eventually undergo structural depletion. Although further work

will be required to test this hypothesis directly, these observations suggest that the loss of upper-layer excitatory neurons may arise secondarily from dysfunction of deep-layer motor circuits.

Moreover, the pattern of vulnerability observed here parallels findings from the SEA-AD cohort, which identified selective depletion of L2/3 IT excitatory neurons in cortical regions (such as the middle temporal gyrus and PFC) in Alzheimer's disease (AD)[21]. Although affecting different cortical areas, these findings suggests that upper-layer excitatory subtypes may represent a shared axis of cortical vulnerability across neurodegenerative disorders.

Notably, in the PFC and PVC, no credible changes in abundance were detected for any cell subtype (Fig. 2d; Supplementary Fig. 2d,e), suggesting that the cellular composition of these regions remains preserved in PD, consistent with the late-stage involvement of both regions in PD pathology.

Collectively, these results highlight the region- and cell-type-specific nature of PD-associated changes in cell type abundance.

Region- and cell-type-specific transcriptional dysregulation in PD is uncoupled from compositional changes

To characterize the transcriptomic response driven by PD at the cell type level across brain regions, we identified differentially expressed genes (DEGs) for each cell subtype and region using a pseudobulk approach (see Methods), comparing PD versus controls and adjusting for technical and demographic covariates (Fig. 3). We found a total of 17,997 unique DEGs (false discovery rate [FDR] $< 5\%$) across all 'cell type $\times$ region' contrasts (Fig. 3a; Supplementary Fig. 5a). DEG yield was highly correlated with cell abundance (Spearman's $\rho = 0.77$, $p < 0.001$), so we modeled this relationship using a non-linear saturation model (Fig. 3b) and computed power-corrected residuals for each contrast as a proxy for transcriptional dysregulation. Using this power-corrected metric, we identified patterns of transcriptional dysregulation that were highly dependent on both brain region and cell type (Fig. 3c) and were uncoupled from the previously identified compositional changes.

In the DMNX, only specific glial populations showed high transcriptional dysregulation, namely both oligodendrocyte subtypes, Astro 2 and Micro 2. None of these transcriptionally affected subtypes were among those exhibiting compositional changes; in fact, the subtypes undergoing structural expansion in the DMNX (Astro 3, Micro 1 and OPCs; Fig. 2a) showed lower than expected dysregulation (i.e., negative residuals). In the GPI, the transcriptional response was contained, with most cell types showing fewer DEGs than expected given their abundance. This included

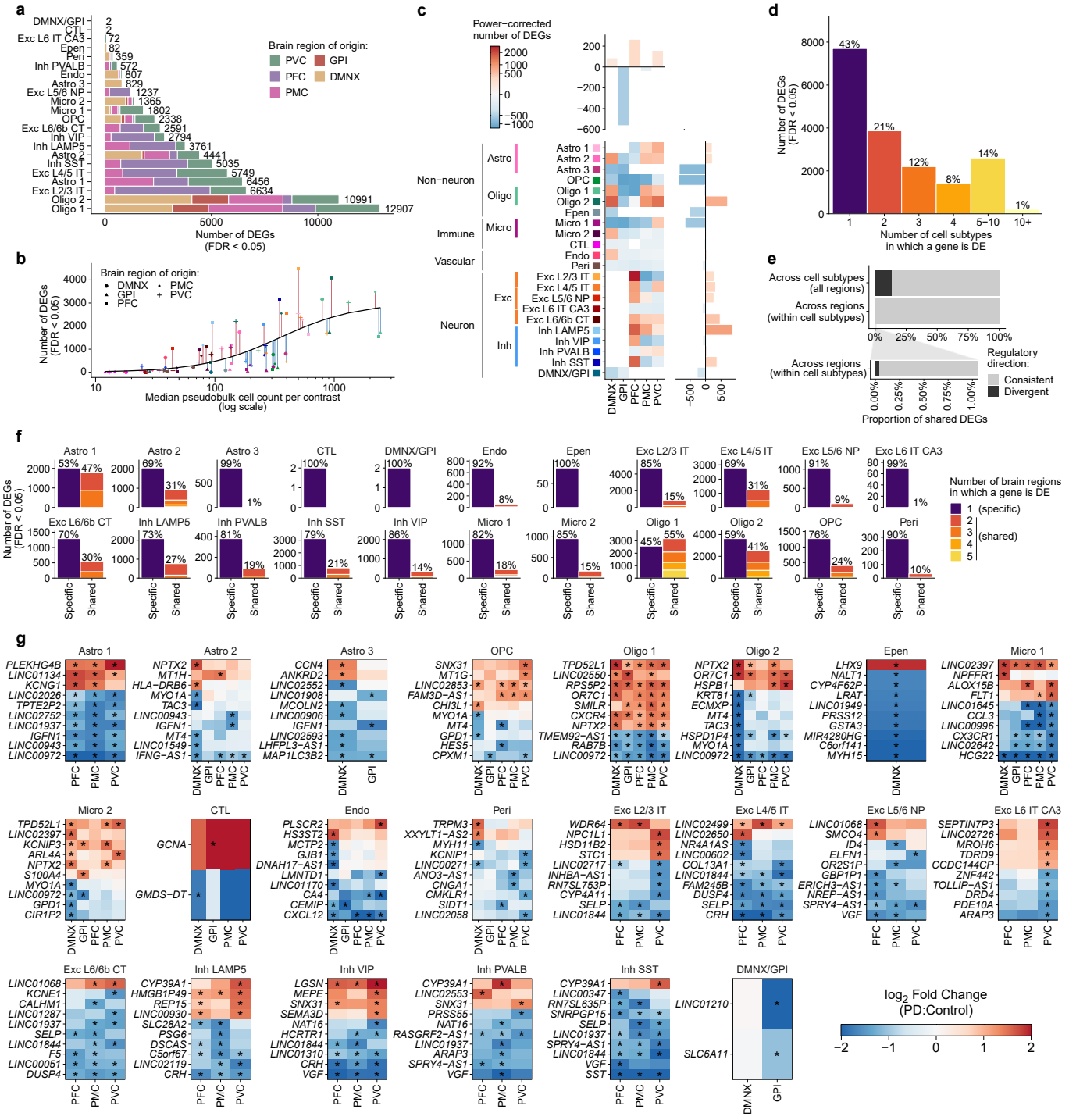


Figure 3: Landscape of differential gene expression in Parkinson's disease.
a Total count of differentially expressed genes (DEGs; FDR $< 5\%$) identified per cell subtype, colored by brain region of origin. Labels indicate the total aggregate DEGs per subtype. **b** Relationship between pseudobulk cell count and differential expression yield. Each point represents a specific cell type-region contrast. The curve depicts a non-linear (Hill) saturation model fitted to the number of DEGs as a function of the median number of cells per pseudobulk profile. Vertical segments represent power-corrected residuals (observed minus predicted DEGs), indicating yields higher (red) or lower (blue) than predicted by cell count alone. **c** Power-corrected differential expression profiles. The heatmap displays the residuals calculated in **b**, illustrating deviations from the expected number of DEGs after accounting for statistical power associated with cell count. Positive values (red) indicate biological dysregulation exceeding statistical expectation, while negative values (blue) indicate fewer DEGs than predicted. Marginal barplots show the mean residual values across brain regions (top) and cell subtypes (right). **d** Cell-type specificity of differential expression. Distribution of DEGs according to the number of cell subtypes in which they are differentially expressed. Percentages indicate the proportion relative to all DEGs. **e** Regulatory consistency. Proportion of shared DEGs showing consistent (light grey) versus divergent (dark grey) fold-change directionality across different cell subtypes (top) or across regions within subtypes (bottom, inset). Divergence is defined as having fold-change estimates with opposite signs in at least two comparisons. **f** Regional specificity within cell subtypes. Stacked bar plots showing the number of DEGs unique to a single brain region (specific; purple) versus those shared across multiple regions (shared; orange/yellow gradient). **g** Top dysregulated genes per cell subtype. Heatmap showing the $\log_2$ fold change (PD vs. control) for the top 10 DEGs with the highest maximum absolute fold change per cell subtype. Genes are ordered by fold change magnitude. Asterisks denote statistical significance (FDR $< 5\%$) in the corresponding region.

the vulnerable Oligo 2 subtype, indicating that despite its significant depletion in the GPI, this population does not exhibit a widespread transcriptional burden. Overall, the GPI emerged as the least transcriptionally affected region (Fig. 3c, top panel).

The PFC was characterized by a clear lineage-specific pattern: while all non-neuronal populations showed lower-than-expected dysregulation, both excitatory and inhibitory neurons exhibited high positive residuals, with Exc L2/3 IT neurons emerging as the most transcriptionally affected population (highest deviation from expected), showing a large proportion of upregulated genes (Supplementary Fig. 5a). This transcriptomic burden in PFC neurons contrasts with the absence of compositional changes there (Fig. 2d). The PMC and PVC displayed a heterogeneous, subtype-dependent response for neuronal populations; in both regions, the transcriptomic burden was primarily driven by glial populations—specifically both oligodendrocyte subtypes, Astro 1, Astro 2 and Micro 1—despite these remaining compositionally stable. The vulnerable excitatory neurons in the PMC did not exhibit a transcriptomic burden beyond expected levels.

Finally, distinct patterns of transcriptional dysregulation became evident across cell types. Both oligodendrocyte subtypes shared a consistent regional burden, with high dysregulation in the DMNX, PMC and PVC, but low dysregulation in the GPI and PFC. In contrast, microglial subtypes exhibited divergent regional vulnerabilities: Micro 1 was highly dysregulated specifically in the PVC, whereas Micro 2 was affected mainly in the DMNX. Conversely, other cell types, such as Astro 3 and OPCs, consistently showed negative residuals across all regions, displaying a limited transcriptomic response characterized by a predominance of downregulated genes (Supplementary Fig. 5a).

Together, these results indicate that transcriptomic alterations in PD are not directly associated with the established spatiotemporal progression of the disease, nor do they mirror compositional changes. Instead, they are highly dependent on cell identity and regional context, revealing that transcriptomic dysregulation and structural vulnerability represent distinct dimensions of the cellular response to PD.

Widespread transcriptional specificity coexists with a conserved core of pan-PD dysregulated genes

Yet quantifying transcriptional burden alone does not reveal whether distinct cell populations converge on shared gene programs. We therefore assessed the cell-type and regional specificity of the PD transcriptional response (Fig. 3d-f). Differential expression was highly cell-type-specific: 43% of DEGs

were restricted to a single subtype, whereas only 1.17% (210 genes) were shared across more than 10 of the 22 subtypes, indicating minimal ubiquity in the PD transcriptomic response (Fig. 3d).

Despite this strong specificity, we identified a robust core of ubiquitous DEGs ('pan-PD markers') consistently dysregulated across diverse cell populations (Supplementary Fig. 5b). Several of these genes have previously been implicated in neurodegeneration, either through functional genomic screenings or transcriptomic studies[22;41–44]. For instance, *DPH6*, *WSB1*, *BNIP3L*, *HP1BP3*, *ANAPC16* and *ZBTB1* have been identified as functional modulators of cellular survival in genome-wide CRISPR interference and activation (CRISPRi/a) screens performed in human brain cell populations[41].

Among these, *BNIP3L* stands out as a particularly relevant candidate: it encodes a key mitophagy receptor required for neuronal survival under basal and stress conditions[41] and may activate a compensatory pathway substituting *PINK1*/*Parkin*-mediated mitochondrial quality control, a mechanism frequently impaired in PD[45–48]. Its widespread upregulation across cell types and brain regions is therefore consistent with broad activation of mitochondrial stress-response programs in PD, extending its pro-survival function beyond neurons. *WSB1*, an E3 ubiquitin ligase regulating LRRK2 ubiquitination and neuronal survival[41;49;50], was consistently downregulated in PD (particularly in neuronal populations), suggesting a potential loss of neuroprotective ubiquitination capacity. *HP1BP3* and *ANAPC16* were consistently upregulated across multiple cell populations, mirroring findings from other studies[22]. Conversely, *DPH6* and *CIRBP* were broadly downregulated. *CIRBP* has recently been proposed as a transcriptomic biomarker of PD[43] and linked to inflammatory regulation in AD[44]. Both *CIRBP* and *DPH6* have been identified as shared hub genes in AD gene regulatory networks[42], suggesting participation in central stress-response mechanisms across neurodegenerative diseases.

We also identified potentially novel and largely uncharacterized mediators of PD. We detected two non-coding transcripts not previously associated with neurodegeneration showing widespread dysregulation across cell types: *LINC00862* (upregulated) and *RFX3-AS1* (downregulated). Although *LINC00862* has been primarily associated with cancer and *SIRT1* regulation[51], its consistent upregulation across diverse cell populations suggests a previously unrecognized role in PD-related stress responses. Although the function of *RFX3-AS1* remains poorly characterized, cancer studies have linked it to proliferative and anti-apoptotic programs[52] and, as an antisense transcript, it may regulate the expression of neighboring genes, including RFX3 and SLC1A1[53].

We further examined the regulatory consistency of shared DEGs. The vast majority of shared genes across cell types displayed consistent directionality, with only 12.9% showing divergent regulation (opposite fold-change signs) (Fig. 3e, top). Such divergences occurred mainly between glial and

neuronal populations (Supplementary Fig. 5c). Notable divergent genes included *MYO5A*[54;55], *DLG2*[56;57] and *NRXN2*[58;59], which were downregulated in PD in glial subtypes (Astro 2, Oligos, Micro, Endo) but upregulated in excitatory and inhibitory neurons; and *SPRED2*[60], which displayed the opposite pattern (upregulated in oligodendrocytes, downregulated in neurons). These divergences highlight that neurons and glial lineages can activate opposing transcriptional programs in response to PD.

Approximately 70% of DEGs within a cell subtype were region-specific, while 30% were shared across at least two regions within the same cell type (Fig. 3f). The most widely shared programs were in oligodendrocytes (Oligo 1: 55% shared; Oligo 2: 41%), Astro 1 (47%) and deep-layer excitatory neurons (∼30%), while populations such as Exc L2/3 IT, Exc L5/6 NP, Astro 3 and microglial subtypes showed highly region-specific profiles; regulatory consistency across regions was extremely high, with sign divergence in only 5 DEGs (<0.1%) (Fig. 3e, bottom; Supplementary Fig. 5d).

Consistent with this high specificity, the most dysregulated genes varied by cell subtype and region (Fig. 3g): neuronal populations showed pronounced downregulation of neuropeptides (*CRH*, *SST*, *VGF*) and upregulation of *CYP39A1* in certain inhibitory subtypes; non-neuronal populations showed alterations in genes linked to autophagic and endolysosomal function (*MAP1LC3B2*, *RAB7B*), immune signaling (*HLA-DRB6*, *CX3CR1*) and chemokine-mediated communication (*CXCL12*, *CXCR4*). Region-specific patterns included selective *MYO1A* downregulation and *NPTX2* upregulation in DMNX glial populations. Notably, lncRNAs (*LINC01844* in neurons, *LINC00972* in glia) emerged as top dysregulated transcripts across multiple lineages.

Beyond individual genes, Gene Set Enrichment Analysis (GSEA) revealed pathway-level signatures across cell types and regions (Supplementary Fig. 6). Protein-folding-related pathways were broadly upregulated in non-neuronal populations across most regions. Mitochondrial ATP synthesis pathways—including oxidative phosphorylation (OXPHOS) and electron transport chain—were dysregulated across cell types with a clear lineage-specific contrast: upregulated in glial populations but downregulated in neurons. Translation-related pathways followed a similar pattern, with broad upregulation in non-neuronal populations and consistent downregulation in neurons. To facilitate full exploration of these extensive results, we developed an interactive web application (`https://juantejedor-pd-atlas-explorer.share.connect.posit.cloud/`) for visualization of gene- and pathway-level findings across all cell subtypes and brain regions.

These results indicate that the transcriptional response to PD is highly dependent on lineage and regional context, with limited overlap in DEG identity but strong conservation in regulatory direction

among shared genes.

A DMNX pathogenic signature dominates cell-type-specific responses in PD

To further dissect the PD transcriptional response across cell types and brain regions, we computed Spearman correlations between logFC profiles across all 'cell type × region' contrasts and applied hierarchical clustering to the resulting correlation matrix (Fig. 4a).

Hierarchical clustering revealed that the transcriptomic response to PD is predominantly organized by cell lineage rather than anatomical location (Fig. 4a).

Nine of the ten clusters were composed exclusively of expression profiles from the same cellular lineage. This was quantitatively supported by partitioning of variance (PERMANOVA[61] on logFC distance matrix): cell subtype identity explained most of the variance ($R^2 = 0.52$, $p < 0.001$), whereas brain region accounted for a smaller fraction ($R^2 = 0.10$, $p < 0.001$), suggesting that cell-type-specific transcriptional signatures are largely conserved across brain regions

One cluster deviated from this pattern, comprising exclusively glial and vascular populations from the DMNX: those populations showed more similar PD-associated transcriptional responses to each other than to their counterparts in other regions, indicating a shared, region-specific pathogenic environment. Principal Component Analysis (PCA) confirmed this, identifying axes of variation specifically associated with DMNX populations (PC5 and PC9; r = 0.54 and r = 0.52, respectively; p < 0.001; Fig. 4b–d).

To characterize the molecular signature underlying the shared DMNX transcriptional responses, we performed GSEA on the genes driving the PCA-derived DMNX axis (Fig. 4e,f), identifying pathways related to mitochondrial function, immune response, neuronal processes, glycosaminoglycan (GAG) biosynthesis and ciliary function—all consistent with the neuropathology of PD.

Decreased activity of mitochondrial respiratory complexes points to bioenergetic failure and oxidative stress, a central feature of PD[62;63]. The prominence of immune pathways (antigen presentation, cytokine signaling and inflammatory responses) supports a neuroinflammatory environment in the early-affected DMNX[64], with TYROBP signaling enrichment further implicating reactive microglia, potentially in response to α-syn aggregates[65;66]. Ciliary-related pathways are consistent with growing evidence that primary cilia in glial cells are altered in PD[67]; notably, mitochondrial dysfunction has been proposed to induce ciliogenesis as a potential adaptive mechanism to reduce

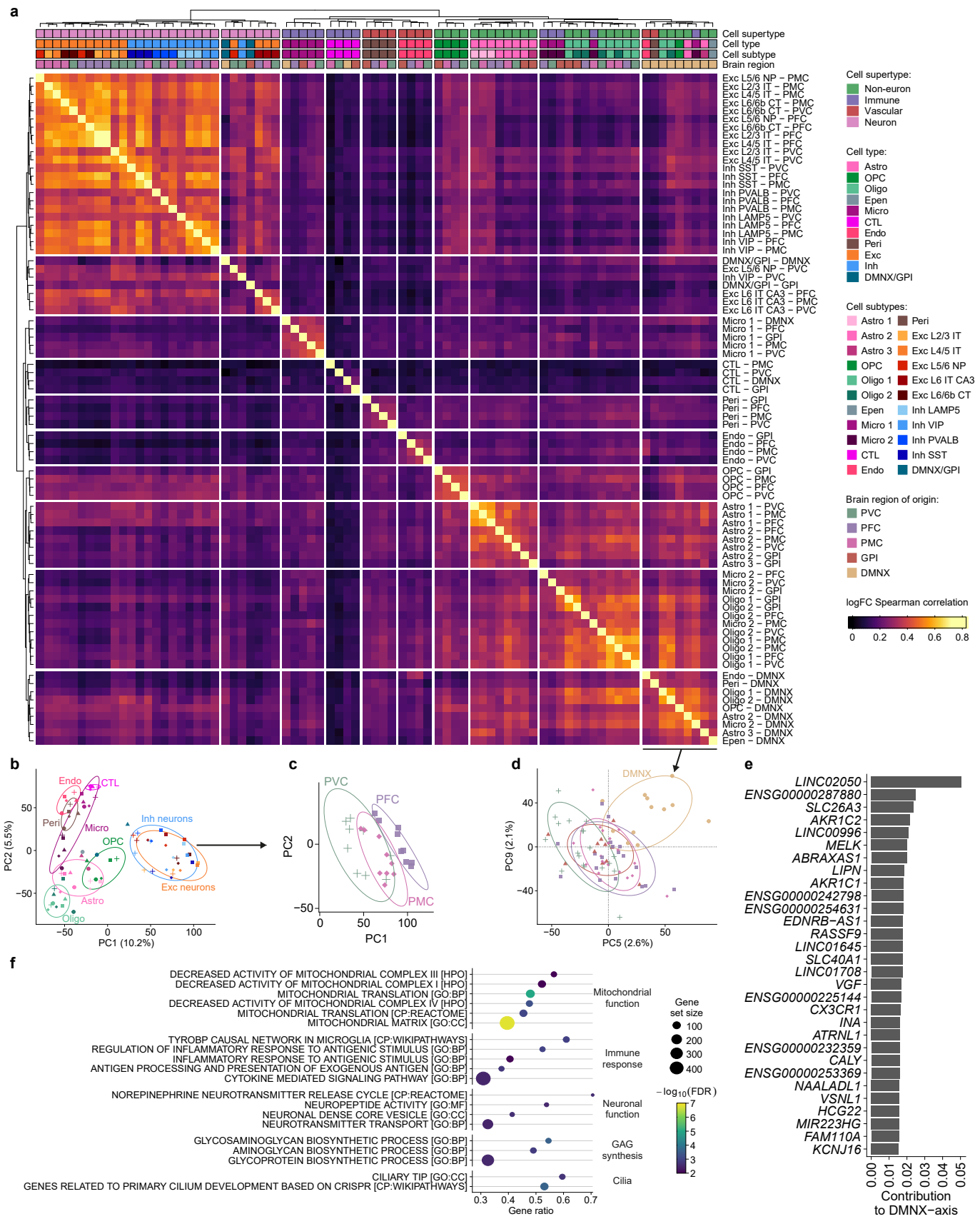


Figure 4: Correlation structure of Parkinson's disease transcriptional responses across cell types and regions. **a** Hierarchical clustering of pairwise Spearman correlations of differential expression profiles ($\log_2$ fold changes) across all cell type-region contrasts. Annotation tracks (top) indicate cell supertype, type, subtype and brain region. **b–c** Principal Component Analysis (PCA) of the pseudobulk ($\log_2$) fold change matrix. Panels display the projection of contrasts onto the first two principal components (PC1 vs. PC2), colored by cell subtype (**b**) or brain region (**c**). Ellipses indicate 80% confidence intervals for cell types (**b**) or regions (**c**). **d** Identification of a DMNX-specific response axis. Projection of contrasts onto PC5 and PC9, which capture a distinct axis of variation separating DMNX (yellow) from other brain regions. **e** Top 30 genes defining the DMNX-specific response, ranked by their weighted loading on the DMNX axis. **f** Functional characterization (GSEA) of the DMNX signature. Displayed terms are restricted to those with a positive Normalized Enrichment Score (NES > 0), reflecting pathways that are specifically enriched among the top-loading genes driving the DMNX response. Dot size represents the number of genes in the set and color indicates statistical significance ($-\log_{10}$ FDR). Pathways are grouped by functional category.

cellular vulnerability[68]. GAG biosynthesis enrichment points to extracellular matrix remodeling; neuroinflammation can promote release of GAGs such as heparan sulfate, implicated in α-syn aggregation and propagation[69;70]. Finally, the involvement of the norepinephrine-signaling pathway is consistent with the known disruption of noradrenergic systems by α-syn pathology[71;72].

Taken together, these findings align closely with PD pathophysiology and indicate that the DMNX axis is driven by a combination of mitochondrial dysfunction, inflammation, extracellular remodeling and altered neuromodulation. This supports a model in which early α-syn pathology in the DMNX establishes a local microenvironment that shapes the transcriptional response across cell types, driving convergence toward shared disease-associated states.

Transcriptomic signatures of selective vulnerability in GPI oligodendrocytes

Given the selective vulnerability of oligodendrocytes in the GPI, we next asked whether transcriptomic differences between subpopulations could explain this susceptibility. Using pseudobulk differential expression and functional enrichment analyses (see Methods), we compared the PD-vulnerable Oligo 2 subtype with the unaffected Oligo 1 subtype (used as an internal control), examining both baseline biological programs and disease-associated responses.

Independent of disease, Oligo 1 showed expression of *OPALIN*, *PLXDC2* and *LINC01608* (Fig. 5a), consistent with previously reported oligodendrocyte markers[73;74], alongside enrichment in pathways related to protein synthesis, RNA splicing and suppression of oligodendrocyte differentiation (Fig. 5b), suggesting a transcriptionally adaptable, less mature state.

In contrast, Oligo 2 expressed markers related to lipid biogenesis (*MBOAT1*[75]) and oligodendrocyte maturation (*TNFRSF21/DR6*[76]) (Fig. 5a), with strong enrichment in lipid metabolism and microtubule-mediated transport pathways (Fig. 5c)— established contributors to myelin synthesis and maintenance[77]— suggesting that Oligo 2 represents a metabolically demanding population engaged in active myelination.

PD-associated pathway changes were highly concordant between oligodendrocyte subtypes ($\rho = 0.77$, $p < 0.001$; Supplementary Fig. 7a): both exhibited upregulation of protein translation, ATP-dependent chaperone-mediated protein folding, OXPHOS and apoptosis-associated signaling, and downregulation of cilium organization and arylsulfatase activity (Supplementary Fig. 7b).

This shared transcriptional signature across subpopulations highlights the engagement of processes commonly implicated in PD pathogenesis, including cellular stress responses, protein quality control

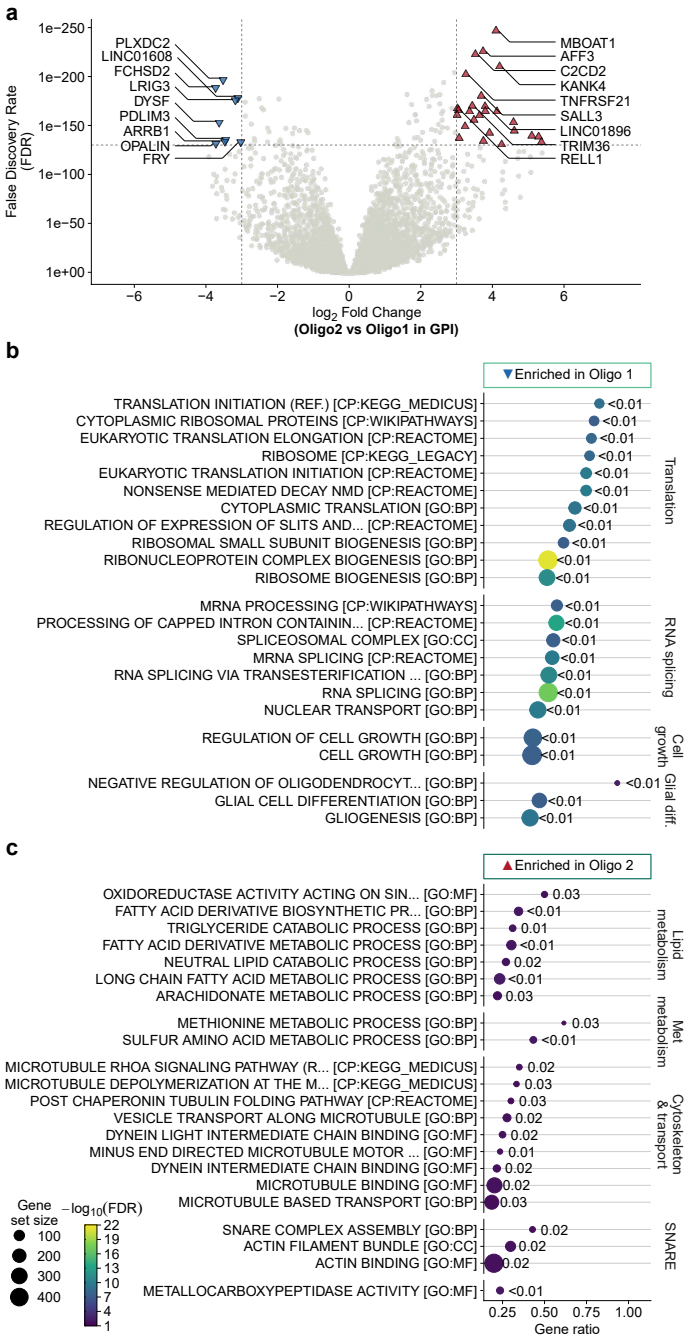


Figure 5: Baseline transcriptomic differences between oligodendrocyte subpopulations in the globus pallidus interna. **a** Volcano plot illustrating biological differential gene expression between the Oligo 2 and Oligo 1 subtypes in the globus pallidus interna (GPI), independent of disease status. Red upward-pointing triangles highlight top genes with significantly higher expression in the Oligo 2 subtype, whereas blue downward-pointing triangles indicate genes with higher expression in the Oligo 1 subtype. **b**–**c** Gene Set Enrichment Analysis (GSEA) characterizing the distinct baseline biological programs of each subpopulation. Displayed are pathways significantly enriched in the resilient Oligo 1 (**b**) and vulnerable Oligo 2 (**c**) subtypes. Dot size represents the number of genes in the set and color indicates statistical significance ($-\log_{10}$ FDR). Pathways are grouped by functional category.

mechanisms and mitochondrial function. Notably, the upregulation of protein synthesis pathways is notable, as cellular stress typically attenuates translation[78]; one plausible explanation is that oligodendrocytes—which produce vast amount of protein to sustain myelin maintenance[79]—may further increase synthesis under PD-related stress to preserve myelination.

The upregulation of ATP-dependent chaperones could reflect the need to fold those newly synthesized proteins or mitigates α-synuclein aggregates[80]. The concurrent increase in OXPHOS may therefore represent a compensatory response to meet the elevated ATP demand—required for both translation and ATP-dependent chaperone activity. This increase in OXPHOS could, in turn, contribute to oxygen depletion, consistent with hypoxia pathway enrichment. Given the known susceptibility of oligodendrocytes to endoplasmic reticulum (ER) stress[79], the combination of increased protein synthesis and elevated OXPHOS—potentially enhancing oxidative stress—may promote the observed apoptotic pathways. Although compensatory responses cannot be distinguished from downstream consequences, these pathways provide a coherent biological link between the upregulation of chaperone folding, OXPHOS, and apoptosis in both subtypes. However, because apoptosis- and stress-related pathways are prominent in both subpopulations, this shared transcriptomic response alone does not explain the selective depletion of Oligo 2 relative to Oligo 1.

To elucidate the basis of this selective vulnerability, we examined the differential response to PD between the two subtypes (the disease-by-subtype interaction, ΔPD Oligo2 vs Oligo1). Only five DEGs were detected (FDR $< 10\%$; Fig. 6a), likely reflecting the correlated responses and limited power of interaction models. Despite minimal gene-level differences, GSEA revealed subtype-specific pathway responses. Under PD, Oligo 1 maintained programs related to RNA metabolism, transcriptional regulation and cellular dedifferentiation (e.g., stem cell proliferation) (Fig. 6b). In contrast, Oligo 2 showed stronger enrichment for IRE1-mediated unfolded protein response (UPR), lipid metabolism and lysosomal acidification (Fig. 6c).

Together, these findings suggest that selective vulnerability may arise from an interplay between intrinsic cellular states and subpopulation-specific stress responses. We hypothesize that the resilient Oligo 1 population leverages its baseline transcriptional adaptability to shift toward a protective, de-differentiated state, thereby tolerating PD-induced stress and avoiding population depletion. Conversely, fully committed, actively myelinating Oligo 2 cells lack this adaptive capacity. This vulnerability may be exacerbated by the physiological demands of the GPI, as a white-matter-dense region requiring intensive myelination[29], the baseline metabolic stress on mature oligodendrocytes is already high[79;81], such that additional PD-induced stress may overwhelm their cellular machinery.

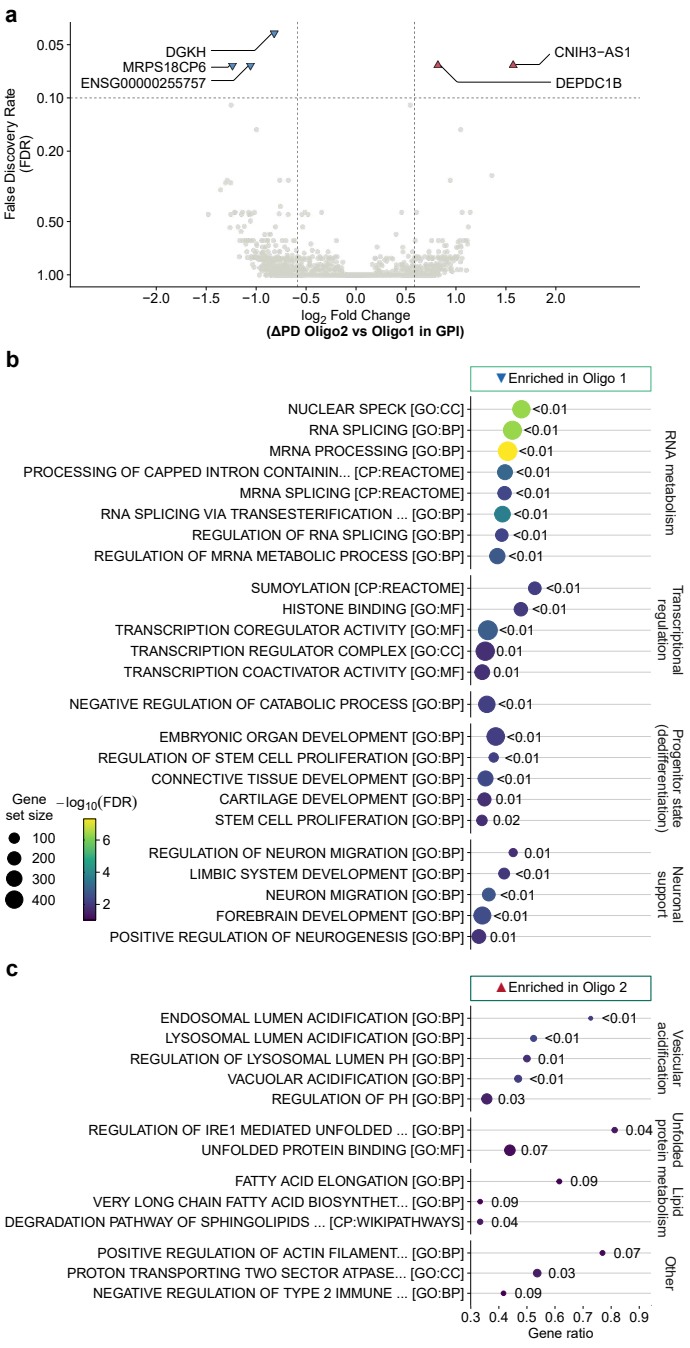


Figure 6: Differential transcriptomic response to Parkinson's disease between oligodendrocyte subpopulations in the globus pallidus interna.
a Volcano plot showing the differential transcriptomic response to PD (disease-by-subtype interaction) between the Oligo 2 and Oligo 1 subtypes in the GPI. Red upward-pointing triangles highlight genes exhibiting a stronger PD-associated response in the Oligo 2 subtype, while blue downward-pointing triangles denote genes with a stronger PD-associated response in the Oligo 1 subtype. **b**–**c** Functional characterization (GSEA) of the subtype-specific responses to PD. Displayed are pathways showing significantly stronger disease-associated enrichment in Oligo 1 (**b**) and Oligo 2 (**c**). Dot size represents the number of genes in the set and color indicates statistical significance ($-\log_{10}$ FDR). Pathways are grouped by functional category.

Consequently, these mature cells become susceptible to unresolved ER stress, leading to sustained, terminal IRE1 activation. Accordingly, observed lysosomal acidification may represent a compensatory crosstalk mechanism to alleviate UPR and support proteostasis[82]; however, if stress remains chronic, prolonged UPR activation can trigger apoptosis[79], contributing to the detected depletion of the Oligo 2 population.

Discussion

This study on the AMP-PD multi-region, cell type-resolved transcriptomic atlas extends beyond the traditional focus on midbrain dopaminergic neuron vulnerability in PD. By analyzing over 2.2 million nuclei across five brain regions, we showed that PD is characterized by alterations extending well beyond the midbrain, affecting both neuronal and glial lineages in a highly region-specific manner.

Shifts in cell type composition were most prominent in the DMNX, an early site of α-syn pathology[3]. Here, we identified a marked expansion of astrocyte, microglial, and OPC subtypes. Furthermore, distinct glial and vascular populations in this region converged toward a shared transcriptional profile characterized by mitochondrial dysfunction, immune signaling and extracellular matrix remodeling, indicating that the early-disease local environment strongly shapes cellular states. In the GPI, we identified the loss of Oligo 2 cells—a population characterized by a transcriptomic profile of reduced resilience to PD-induced proteostatic stress. This finding aligns with recent single-nuclei data from the PD midbrain[6] and reinforces the emerging concept that oligodendrocyte dysfunction and altered myelination are core components of PD pathogenesis. Finally, in the neocortex, we observed a selective depletion of layer 2/3 intratelencephalic excitatory neurons in the PMC. This cortical vulnerability is consistent with findings in Alzheimer's disease, where supragranular excitatory populations are similarly affected[21], and correlates with the progression of cortical motor and cognitive deficits in PD.

Despite this regional heterogeneity, we identified a consistent transcriptomic signature associated with cellular stress across diverse regions and cell types, including alterations in *BNIP3L* and *WSB1*. Beyond protein-coding genes, we detected previously unreported non-coding transcripts broadly altered in PD, including *LINC00862* and *RFX3-AS1*, highlighting a potentially underexplored role for non-coding RNAs in PD-related cellular stress responses.

This atlas provides a reference for the cellular and molecular alterations underlying PD across multiple brain regions. By coupling these findings with our interactive web application, this work offers an accessible framework for further targeted investigations into the pathogenesis of PD.

Methods

AMP-PD snRNA-seq cohort and preprocessing

The single-nucleus transcriptomic data analyzed in this study, together with the associated clinical, demographic and neuropathological metadata, were obtained from version 4 of the AMP-PD consortium dataset, comprising post-mortem brain tissue from 97 donors across five brain regions (444 samples, 2,441,192 nuclei). A full description of study design, cohort composition, tissue collection, snRNA-seq library preparation and primary computational preprocessing is provided in N. M. et al.[9].

snRNA-seq normalization, integration and clustering

All downstream analyses in this study were performed de novo starting from the preprocessed gene expression matrix provided by the AMP-PD consortium, prior to any clustering, annotation or cluster-level filtering steps described in N. M. et al.[9].

We performed downstream processing using the Scanpy[83] (v1.11.0) Python package. We normalized the preprocessed count matrix by scaling counts to the median library size (`scanpy.pp.normalize_total()`, `target_sum=None`) followed by $\log(x + 1)$ transformation (`scanpy.pp.log1p()`). We identified highly variable genes (HVGs) using the Seurat v3 flavor (`scanpy.pp.highly_variable_genes()`), selecting the top 20% most variable. We computed Principal Component Analysis (PCA) on the normalized expression of the 8,000 HVGs selected using `scanpy.pp.pca()`. Based on the variance explained (elbow method), we selected the top 50 principal components (PCs) for downstream analysis.

To correct for technical and biological batch effects, including source brain bank, sequencing batch and donor identity, we performed data integration using Harmony[84] at the donor level on the top 50 PCs (`scanpy.external.pp.harmony_integrate()`, `key="participant_id"`). We constructed a k-nearest-neighbor graph using Manhattan distance on the Harmony-corrected PCs (`scanpy.pp.neighbors()`, `k=30`). We carried out unsupervised clustering using the Leiden algorithm[85] (`scanpy.tl.leiden()`, `resolution=0.25`). We performed dimensionality reduction for visualization using Uniform Manifold Approximation and Projection (UMAP)[86] with a minimum distance of 0.1.

We detected potential doublets using Scrublet[87] (`scanpy.pp.scrublet()`) based on the 50 PCs. In addition, we excluded clusters dominated by nuclei originating from a single donor or a very small

number of samples. After quality control, the final dataset comprised 2,404,063 nuclei.

Cell type annotation

We implemented a multi-stage strategy to characterize cell types for each Leiden cluster. First, we performed automated label transfer using `scanpy.tl.ingest()` with the BRAIN Initiative Cell Census Network (BICCN) whole human brain atlas as a reference[10]. To improve annotation specificity, we filtered the reference dataset from 3 million to approximately 1 million nuclei, keeping only dissections anatomically matched to the AMP-PD sampled regions (medulla, basal forebrain, frontal/parietal cortex and occipital cortex). We additionally used the SEA-AD Alzheimer's atlas[88] as a secondary reference to validate clusters with ambiguous identities (particularly among excitatory neuron subtypes) using MapMyCells[89] for label transfer. Finally, annotations were assigned to each Leiden cluster based on the dominant transferred cell type label.

To refine these annotations, we performed pseudobulk differential expression analysis (DEA) to identify cluster-specific marker genes. We aggregated counts by cluster using decoupleR (v.2.0.4) Python package[90](`decoupler.pp.pseudobulk()`, `mode="sum"`) and we assessed differential expression using `edgeR`[91] in R. We filtered lowly expressed genes (`edgeR::filterByExpr()` with `min_count=1`, `min_total_count=50`, `min_prop=0.85`) and normalized library sizes (`normLibSizes()`). We fitted a negative binomial generalized linear model (NB-GLM) for each gene using the function `edgeR::glmQLFit()` with `robust=TRUE`. The model formula was specified as $\sim$ cluster+age at death+ PMI + sex + brain bank. We computed one-vs-rest contrasts to derive marker genes for each cluster. We derived final cell type annotations by integrating data-driven markers with established literature-based markers[12–15].

While we used the full cohort ($\approx$ 2.4 million nuclei from 97 donors) for integration and annotation, we excluded donors with non-PD neurodegenerative disorders (3 with parkinsonism and 1 with dementia with Lewy bodies) from subsequent comparative analyses (i.e. differential composition and expression), yielding a final dataset of 2,280,473 nuclei from 429 samples across 93 donors (69 PD, 24 controls).

PD differential cell subtype composition analysis

To identify changes in cell type composition between PD donors and healthy controls, we employed tascCODA[20], a Bayesian compositional method that extends scCODA[19] to incorporate tree-structured

relationships among cell types, implemented in the pertpy[92] (v1.0.0) Python package.This approach was chosen because cell count data are compositional: under the sum-to-one constraint, an increase in one cell type proportion necessarily decreases the others, potentially inflating false-positive discoveries if unaccounted for[19]. The tascCODA framework models these compositional changes between conditions while simultaneously accounting for the hierarchical relationships among cell types and incorporating sample-level covariates.

The compositional analysis was performed independently for each of the five brain regions. For each region, we created a separate AnnData object containing cell counts aggregated by subtype and donor. The tascCODA model uses these raw counts as direct input, inherently accounting for the compositional nature of the data by modeling their relative proportions. The region-specific cell type hierarchy (supertype, type and subtype) was incorporated into each AnnData object (`pertpy.tl.Tasccoda().load()` with `type="sample_level"`). We tested for compositional changes associated with disease status while controlling for brain bank, sex and age. The model formula was specified for the function `pertpy.tl.Tasccoda().prepare()` as '$\sim$ disease status + sex + age at death + brain bank', with age at death rescaled to a 0-1 range. To prioritize detection of changes in specific cell subtypes over broader lineage-level changes, we set the node-adaptive penalization parameter (ϕ) to 5. Posterior distributions of model parameters were estimated using a No-U-Turn Sampler (NUTS) for Markov chain Monte Carlo (MCMC) sampling, using the function `pertpy.tl.Tasccoda().run_nuts()` with 2,000 warm-up and 10,000 sampling iterations. Accordingly, within this Bayesian framework, compositional changes reported as 'credible' correspond to effects (model coefficients) whose posterior median exceeded the threshold of practical significance (see Equations 11-13 in ref.[20]), rather than through p-value-based significance testing.

A critical step in this analysis is the selection of a reference cell type, which is assumed to be compositionally invariant across all covariates. As the true stability of any cell type was unknown a priori, we implemented a two-stage procedure for reference selection. First, to enable the investigation of our primary cell types of interest, we excluded all neuronal and glial subtypes from the pool of potential references. Second, to empirically identify the most suitable reference, we systematically executed the model for each region using every remaining subtype as the reference, yielding a total of 80 models per region. This iterative process allowed us to assess the consistency of credible effects irrespective of the reference chosen and to identify the most invariant cell type, defined as the subtype with the lowest frequency of credible associations across all covariates and model runs. For each cell type-covariate pair, we quantified the consistency of an association as the proportion of valid models

in which it was detected. A model was considered invalid for assessing a specific cell type if the chosen reference was one of its hierarchical descendants, as this constraint forces the parent node's effect to zero.

This systematic evaluation confirmed that vascular cells were the most stable, with endothelial cells and pericytes showing the fewest significant associations. Between these two candidates, pericytes were selected as the final reference as their relative abundance exhibited a lower coefficient of variation across samples compared to endothelial cells. All subsequently reported quantitative metrics and parameter estimates were derived from the definitive model using pericytes as the reference cell type.

Throughout the main text, we refer to two distinct effect sizes: the 'effect size', corresponding to the node-level parameter directly inferred for each node in the cell type hierarchy, and the 'propagated effect size', obtained by aggregating credible node-level effects across all ancestors of a given cell subtype. Additionally, to facilitate interpretation in the main text, model-predicted $\log_2$ FC values were converted to percentage changes in relative abundance using the formula $|2^{\log_2 \mathrm{FC}} - 1| \times 100$. A detailed description of how these metrics are derived and their meaning is provided in Supplementary Note 1.

PD differential gene expression

To identify transcriptomic changes associated with PD, we performed a pseudobulk DEA comparing PD donors against healthy controls.

We generated pseudobulk profiles by aggregating counts (`dc.pp.pseudobulk()`, `mode="sum"`) for each unique combination of donor, brain region and cell subtype, resulting in an initial set of 8,140 profiles. We excluded donors with missing PMI and profiles containing fewer than 10 nuclei or representing cell subtype-region combinations contributing less than 5% of the total abundance of that subtype across all regions. This filtering resulted in 5,848 pseudobulk profiles.

We filtered lowly expressed genes for each cell subtype using `edgeR::filterByExpr()` with `min_count=1`, `min_total_count=50` and `min_prop=0.85`. We computed normalization factors using the 'TMMwsp' method in `edgeR::calcNormFactors`, which accounts for data with high sparsity.

We modeled differential expression independently for each cell subtype using the `limma`[93] package in R. We fitted a linear model using `limma::voomLmFit()` enabling precision weighting (`sample.weights=TRUE`) to account for heteroscedasticity and a random effect for the donor (`block=participant_id`) to account for the correlation structure of multiple brain regions sampled

from the same individual.

Exploratory PCA revealed residual effects of library size on the first principal component; therefore, we explicitly included library size as a covariate. The final model design was specified as '$\sim$ group + scale(log(1 + lib. size)) + scale(age at death) + scale(PMI) + sex + brain bank' where the *group* term represents the interaction between brain region and disease status, enabling region-specific contrasts between PD cases and controls.

To characterize the biological processes underlying the PD transcriptional response at the pathway level, we performed GSEA for each cell subtype-region contrast. Gene sets were obtained from the Molecular Signatures Database (MSigDB) via the `msigdbr` package[96]. Gene sets with fewer than 10 or more than 500 genes were excluded. For each contrast, genes were ranked by their moderated t-statistic and GSEA was applied using the `GSEA()` function from the `clusterProfiler` package[95].

Power correction of differential expression yield

To account for the confounding effect of cell abundance (statistical power) on the number of detected DEGs, we modeled the relationship between DEG yield and pseudobulk cell counts. For each 'cell subtype $\times$ brain region' contrast, we calculated the median number of cells across the pseudobulk profiles included in that contrast. We fitted a non-linear saturation model (Hill equation) using the `nls()` function in R, defined as:

$$y_i = \frac{\alpha \cdot x_i^n}{\beta^n + x_i^n}$$

where y_i is the number of significant DEGs (FDR < 0.05) for the i-th contrast, x_i is the median pseudobulk cell count for that contrast, α represents the asymptotic maximum number of DEGs and β represents the cell count at half-maximal yield.

We computed power-corrected transcriptomic dysregulation scores (residuals) by subtracting the model-predicted number of DEGs from the observed number of DEGs. Positive residuals indicate a transcriptomic dysregulation burden greater than expected by statistical power alone, while negative residuals indicate a relatively preserved transcriptomic state. Finally, to evaluate the direction of regulation, these residuals were proportionally partitioned into upregulated and downregulated fractions based on the original ratio observed in that specific contrast.

Comparative analysis of transcriptomic responses

To compare the transcriptomic response to PD across diverse cellular and regional contexts, we analyzed differential expression profiles constructing a matrix of $\log_2$ FC values (PD vs control) for all genes across all 'cell subtype × brain region' contrasts. We quantified pairwise similarities between transcriptomic profiles using Spearman correlation. We performed hierarchical clustering of the expression profiles on the distance matrix defined as '1 − Spearman correlation', using Ward's minimum variance method (`ward.D2`). To quantify the proportion of variance in transcriptomic responses explained by cell lineage and brain region, we performed a permutational multivariate analysis of variance (PERMANOVA) on the distance matrix using the `adonis2()` function from the `vegan` package[94], assessing marginal effects (`by="margin"`).

We performed PCA on the $\log_2$ FC matrix using `prcomp()`. To prevent transcriptomic profiles with extreme FC values from dominating the PCs, profiles were centered and scaled.

To functionally characterize the pathways driving the DMNX transcriptomic convergence, we selected PCs significantly associated ($p < 0.001$) with DMNX by performing a correlation test between PC scores and the profile regional identity. Then, we constructed a DMNX-composite axis by averaging the gene loadings from the significantly associated PCs. Finally, we performed a GSEA on genes ranked in descending order by their composite loading, following the same procedure described above. Pathways with an FDR $< 1\%$ and a NES > 0 were considered significantly enriched among the top-loading genes.

Differential transcriptomic characterization of GPI oligodendrocyte subpopulations

To characterize the transcriptomic signatures underlying selective oligodendrocyte vulnerability in the GPI, we applied the pseudobulk DEA pipeline described above to a subsetted matrix containing exclusively Oligo 1 and Oligo 2 profiles from this region. Within the `limma` framework, to dissect both the intrinsic biological differences and the pathological responses to PD, we extracted four linear contrasts from the model:

1. **Global biological differences:** $\frac{1}{2}(\text{Oligo } 2_{\text{PD}} + \text{Oligo } 2_{\text{Control}}) - \frac{1}{2}(\text{Oligo } 1_{\text{PD}} + \text{Oligo } 1_{\text{Control}})$; referred to as 'Oligo2 vs Oligo1'.

2. **Oligo 1-specific PD response:** $\text{Oligo } 1_{\text{PD}} - \text{Oligo } 1_{\text{Control}}$

3. **Oligo 2-specific PD response:** Oligo 2_{PD} − Oligo 2_{Control}

4. **Differential PD response (interaction):** (Oligo 2_{PD}−Oligo 2_{Control})−(Oligo 1_{PD}−Oligo 1_{Control}); referred to as 'ΔPD Oligo2 vs Oligo1'.

Functional characterization of these results followed the GSEA methodology detailed above, using the moderated t-statistic of each contrast as the ranking metric.

Data availability

The single-nucleus RNA sequencing data analyzed in this study were obtained from the Accelerating Medicines Partnership® Parkinson's Disease (AMP PD) Knowledge Platform (https://www.amp-pd.org). The dataset used corresponds to v4.0 of 'Postmortem Sequencing Data'.

Additionally, the interactive web application built to navigate the differential expression and functional enrichment results across all cell types and regions is freely accessible at https://juantejedor-pd-atlas-explorer.share.connect.posit.cloud/.

Code availability

All code used for data preprocessing, statistical analyses and figure generation is available on GitHub at https://github.com/BiostatOmics/TejedorSerrano2026-pd-atlas. A snapshot of the repository corresponding to the version used in this manuscript has been archived at Zenodo https://doi.org/10.5281/zenodo.20381091.

Acknowledgements

Data used in the preparation of this article were obtained from the Accelerating Medicines Partnership® (AMP®) Parkinson's Disease (AMP PD) and Parkinson's Disease & Related Disorders (AMP PDRD) Knowledge Platform Knowledge Platform. For up-to-date information on the study, visit https://www.amp-pdrd.org.

The AMP® PD program is a public-private partnership managed by the Foundation for the National Institutes of Health and funded by the National Institute of Neurological Disorders and Stroke (NINDS) in partnership with the Food and Drug Administration (FDA), National Institute on Aging (NIA), Aligning Science Across Parkinson's (ASAP) initiative; Celgene Corporation, a

subsidiary of Bristol-Myers Squibb Company; GlaxoSmithKline plc (GSK); The Michael J. Fox Foundation for Parkinson's Research (MJFF); AbbVie Inc.; Pfizer Inc.; Sanofi US Services Inc.; and Verily Life Sciences LLC.

The AMP® PDRD program is a public-private partnership managed by the Foundation for the National Institutes of Health and funded by the National Institute of Neurological Disorders and Stroke (NINDS) in partnership with the Food and Drug Administration (FDA), National Institute on Aging (NIA), AbbVie Inc.; Aligning Science Across Parkinson's (ASAP) initiative; C2N Diagnostics, LLC; CurePSP; GlaxoSmithKline plc (GSK); Denali Therapeutics Inc.; Laboratory Corporation of America Holdings (Labcorp); The Michael J. Fox Foundation for Parkinson's Research (MJFF); Sanofi US Services Inc.; and Verily Life Sciences LLC.

ACCELERATING MEDICINES PARTNERSHIP and AMP are registered service marks of the U.S. Department of Health and Human Services.

Postmortem brain tissue data used in preparation of this article were obtained by the Mount Sinai Brain Bank, University of Miami Brain Endowment Bank, Harvard Brain Tissue Resource Center, and the Udall Center of Excellence for Parkinson's Disease Research, accessed via the AMP PD platform.

This work was funded by FEDER/Junta de Andalucía-Consejería de Universidad, Investigación e Innovación (ProyExcel_00978) and by the Spanish MICIU (PID2023-152976NB-I00). J.A.T.S was supported by the Spanish Ministry of Universities through the FPU fellowship program FPU23/01866. J.M.M. was supported by Grant RYC2024-049532-I funded by MICIU/AEI/10.13039/501100011033 and by 'ESF+'. A.A.L. was supported by Grant JDC2024-053114-I funded by MICIU/AEI/10.13039/501100011 and by 'ESF+'.

The authors thank the Supercomputing and Bioinnovation Center (SCBI) of the University of Malaga for their provision of computational resources (the supercomputer Picasso) and technical support (www.scbi.uma.es/site).

Author contributions

- J.A.T.S.: Conceptualization, Formal analysis, Investigation, Methodology, Software, Visualization, Writing - original draft, Writing - review & editing.
- A.A.L.: Conceptualization, Supervision, Writing - review & editing.

- S.T.: Conceptualization, Supervision, Funding acquisition, Writing - review & editing.
- J.M.M.: Conceptualization, Data curation, Resources, Supervision, Funding acquisition, Writing - review & editing.

Competing interests

The authors declare no competing interests.

References

[1] Poewe, W. *et al.* Parkinson disease. *Nature Reviews Disease Primers* **3**, 1–21 (2017).

[2] Obeso, J. *et al.* Past, present, and future of Parkinson's disease: A special essay on the 200th Anniversary of the Shaking Palsy. *Movement Disorders* **32**, 1264–1310 (2017).

[3] Braak, H. *et al.* Staging of brain pathology related to sporadic Parkinson's disease. *Neurobiology of Aging* **24**, 197–211 (2003).

[4] Kamath, T. *et al.* Single-cell genomic profiling of human dopamine neurons identifies a population that selectively degenerates in Parkinson's disease. *Nature Neuroscience* **25**, 588–595 (2022).

[5] Agarwal, D. *et al.* A single-cell atlas of the human substantia nigra reveals cell-specific pathways associated with neurological disorders. *Nature Communications* **11**, 4183 (2020).

[6] Smajić, S. *et al.* Single-cell sequencing of human midbrain reveals glial activation and a Parkinson-specific neuronal state. *Brain* **145**, 964–978 (2021).

[7] Liu, C. *et al.* Brain Functional and Structural Signatures in Parkinson's Disease. *Frontiers in Aging Neuroscience* **12**, 125 (2020).

[8] Panicker, N., Ge, P., Dawson, V. L. & Dawson, T. M. The cell biology of Parkinson's disease. *The Journal of Cell Biology* **220**, e202012095 (2021).

[9] N. M., P. *et al.* A multi-region single nucleus transcriptomic atlas of Parkinson's disease. *Scientific Data* **11**, 1274 (2024).

[10] Siletti, K. *et al.* Transcriptomic diversity of cell types across the adult human brain. *Science* **382**, eadd7046 (2023).

[11] von Bartheld, C. S., Bahney, J. & Herculano-Houzel, S. The search for true numbers of neurons and glial cells in the human brain: A review of 150 years of cell counting. *Journal of Comparative Neurology* **524**, 3865–3895 (2016).

[12] Chen, X. *et al.* A brain cell atlas integrating single-cell transcriptomes across human brain regions. *Nature Medicine* **30**, 2679–2691 (2024).

[13] Hodge, R. D. *et al.* Conserved cell types with divergent features in human versus mouse cortex. *Nature* **573**, 61–68 (2019).

[14] Tasic, B. *et al.* Shared and distinct transcriptomic cell types across neocortical areas. *Nature* **563**, 72–78 (2018).

[15] Yao, Z. *et al.* A transcriptomic and epigenomic cell atlas of the mouse primary motor cortex. *Nature* **598**, 103–110 (2021).

[16] Werner, M. S. *et al.* Chromatin-enriched lncRNAs can act as cell-type specific activators of proximal gene transcription. *Nature Structural & Molecular Biology* **24**, 596–603 (2017).

[17] Derrien, T. *et al.* The GENCODE v7 catalog of human long noncoding RNAs: Analysis of their gene structure, evolution, and expression. *Genome Research* **22**, 1775–1789 (2012).

[18] Liu, S. J. *et al.* Single-cell analysis of long non-coding RNAs in the developing human neocortex. *Genome Biology* **17**, 67 (2016).

[19] Büttner, M., Ostner, J., Müller, C. L., Theis, F. J. & Schubert, B. scCODA is a Bayesian model for compositional single-cell data analysis. *Nature Communications* **12**, 6876 (2021).

[20] Ostner, J., Carcy, S. & Müller, C. L. tascCODA: Bayesian Tree-Aggregated Analysis of Compositional Amplicon and Single-Cell Data. *Frontiers in Genetics* **12**, 766405 (2021).

[21] Gabitto, M. I. *et al.* Integrated multimodal cell atlas of Alzheimer's disease. *Nature Neuroscience* **27**, 2366–2383 (2024).

[22] Martirosyan, A. *et al.* Unravelling cell type-specific responses to Parkinson's Disease at single cell resolution. *Molecular Neurodegeneration* **19**, 7 (2024).

[23] Dehestani, M. *et al.* Transcriptomic changes in oligodendrocytes and precursor cells associate with clinical outcomes of Parkinson's disease. *Molecular Brain* **17**, 56 (2024).

[24] Sorrentino, Z. A. *et al.* Intrastriatal injection of α-synuclein can lead to widespread synucleinopathy independent of neuroanatomic connectivity. *Molecular Neurodegeneration* **12**, 40 (2017).

[25] Gleason, D., Fallon, J. H., Guerra, M., Liu, J. C. & Bryant, P. J. Ependymal stem cells divide asymmetrically and transfer progeny into the subventricular zone when activated by injury. *Neuroscience* **156**, 81–88 (2008).

[26] Bae, E.-J., Pérez-Acuña, D., Rhee, K. H. & Lee, S.-J. Changes in oligodendroglial subpopulations in Parkinson's disease. *Molecular Brain* **16**, 65 (2023).

[27] Salvesen, L. *et al.* Changes in total cell numbers of the basal ganglia in patients with multiple system atrophy - A stereological study. *Neurobiology of Disease* **74**, 104–113 (2015).

[28] Cheng, D. *et al.* Explainable classification of Parkinson's disease with different motor subtypes by analyzing the synthetic MRI quantitative parameters of subcortical nuclei. *European Journal of Radiology* **190**, 112272 (2025).

[29] Lanciego, J. L., Luquin, N. & Obeso, J. A. Functional Neuroanatomy of the Basal Ganglia. *Cold Spring Harbor Perspectives in Medicine* **2**, a009621 (2012).

[30] Kaya, I. *et al.* Spatial lipidomics reveals brain region-specific changes of sulfatides in an experimental MPTP Parkinson's disease primate model. *npj Parkinson's Disease* **9**, 118 (2023).

[31] Halliday, G. M., Macdonald, V. & Henderson, J. M. A comparison of degeneration in motor thalamus and cortex between progressive supranuclear palsy and Parkinson's disease. *Brain* **128**, 2272–2280 (2005).

[32] Swanson, O. K., Semaan, R. & Maffei, A. Reduced Dopamine Signaling Impacts Pyramidal Neuron Excitability in Mouse Motor Cortex. *eneuro* **8**, ENEURO.0548–19.2021 (2021).

[33] Chen, L., Daniels, S., Kim, Y. & Chu, H.-Y. Cell Type-Specific Decrease of the Intrinsic Excitability of Motor Cortical Pyramidal Neurons in Parkinsonism. *The Journal of Neuroscience* **41**, 5553–5565 (2021).

[34] MacDonald, V. & Halliday, G. M. Selective loss of pyramidal neurons in the pre-supplementary motor cortex in Parkinson's disease. *Movement Disorders* **17**, 1166–1173 (2002).

[35] Fu, Y. *et al.* Adaptive structural changes in the motor cortex and white matter in Parkinson's disease. *Acta Neuropathologica* **144**, 861–879 (2022).

[36] Braak, H. & Del Tredici, K. Neuroanatomy and pathology of sporadic Parkinson's disease. *Advances in Anatomy, Embryology, and Cell Biology* **201**, 1–119 (2009).

[37] Goralski, T. M. *et al.* Spatial transcriptomics reveals molecular dysfunction associated with cortical Lewy pathology. *Nature Communications* **15**, 2642 (2024).

[38] Chen, L., Chehade, H. D. & Chu, H.-Y. Motor cortical neuronal hyperexcitability associated with α-synuclein aggregation. *npj Parkinson's Disease* **11**, 18 (2025).

[39] McColgan, P., Joubert, J., Tabrizi, S. J. & Rees, G. The human motor cortex microcircuit: insights for neurodegenerative disease. *Nature Reviews Neuroscience* **21**, 401–415 (2020).

[40] Pasquereau, B. & Turner, R. S. Primary motor cortex of the parkinsonian monkey: differential effects on the spontaneous activity of pyramidal tract-type neurons. *Cerebral Cortex* **21**, 1362–1378 (2011).

[41] Tian, R. *et al.* Genome-wide CRISPRi/a screens in human neurons link lysosomal failure to ferroptosis. *Nature Neuroscience* **24**, 1020–1034 (2021).

[42] Liu, D. *et al.* From correlation to causation: cell-type-specific gene regulatory networks in Alzheimer's disease. *Alzheimer's & Dementia* **22**, e71053 (2026).

[43] Wang, H. *et al.* Bioinformatics analysis to explore biomarkers and mechanisms of action associated with endoplasmic reticulum stress and ferroptosis in Parkinson's disease. *PLOS ONE* **20**, e0328682 (2025).

[44] Li, Z. *et al.* Cold Inducible RNA-Binding Protein Promotes the Development of Alzheimer's Disease Partly by Inhibition of uPA in Astrocytes. *Degenerative Neurological and Neuromuscular Disease* **14**, 143–155 (2024).

[45] Gao, F. *et al.* The mitochondrial protein BNIP3L is the substrate of PARK2 and mediates mitophagy in PINK1/PARK2 pathway. *Human Molecular Genetics* **24**, 2528–2538 (2015).

[46] Koentjoro, B., Park, J.-S. & Sue, C. M. Nix restores mitophagy and mitochondrial function to protect against PINK1/Parkin-related Parkinson's disease. *Scientific Reports* **7**, 44373 (2017).

[47] Li, Y. *et al.* BNIP3L/NIX-mediated mitophagy: molecular mechanisms and implications for human disease. *Cell Death & Disease* **13**, 14 (2021).

[48] Kakoty, V., Goh, K. W., Kesharwani, P. & Ko, Y. T. BNIP3L/NIX-mediated mitophagy: Future directions in Alzheimer's disease. *Brain Research* **1867**, 149970 (2025).

[49] Nucifora, F. C. *et al.* Ubiqutination via K27 and K29 chains signals aggregation and neuronal protection of LRRK2 by WSB1. *Nature Communications* **7**, 11792 (2016).

[50] Haque, M., Kendal, J. K., MacIsaac, R. M. & Demetrick, D. J. WSB1: from homeostasis to hypoxia. *Journal of Biomedical Science* **23**, 61 (2016).

[51] Liu, S. *et al.* Pan-cancer analysis of super-enhancer-induced LINC00862 and validation as a SIRT1-promoting factor in cervical cancer and gastric cancer. *Translational Oncology* **45**, 101982 (2024).

[52] Hu, Y. *et al.* Long noncoding RNA regulatory factor X3- antisense RNA 1 promotes non-small cell lung cancer via the microRNA-577/signal transducer and activator of transcription 3 axis. *Bioengineered* **13**, 10749–10764 (2022).

[53] Ham, J. *et al.* Ginsenoside Rg3 and Korean Red Ginseng extract epigenetically regulate the tumor-related long noncoding RNAs RFX3-AS1 and STXBP5-AS1. *Journal of Ginseng Research* **43**, 625–634 (2019).

[54] Gupta, R. & Kumar, P. CREB1K292 and HINFPK330 as Putative Common Therapeutic Targets in Alzheimer's and Parkinson's Disease. *ACS Omega* **6**, 35780–35798 (2021).

[55] Landrock, K. K. *et al.* Pleiotropic neuropathological and biochemical alterations associated with Myo5a mutation in a rat Model. *Brain Research* **1679**, 155–170 (2018).

[56] Zhao, A. *et al.* SNPs in SNCA, MCCC1, DLG2, GBF1 and MBNL2 are associated with Parkinson's disease in southern Chinese population. *Journal of Cellular and Molecular Medicine* **24**, 8744–8752 (2020).

[57] Wu, H.-C. *et al. DLG2*, but not *TMEM229B*, *GPNMB*, and *ITGA8* polymorphism, is associated with Parkinson's disease in a Taiwanese population. *Neurobiology of Aging* **64**, 158.e1–158.e6 (2018).

[58] Cuttler, K., Hassan, M., Carr, J., Cloete, R. & Bardien, S. Emerging evidence implicating a role for neurexins in neurodegenerative and neuropsychiatric disorders. *Open Biology* **11**, 210091 (2021).

[59] Cuttler, K. *et al.* Neurexin 2 p.G849D variant, implicated in Parkinson's disease, increases reactive oxygen species, and reduces cell viability and mitochondrial membrane potential in SH-SY5Y cells. *Journal of Neural Transmission* **129**, 1435–1446 (2022).

[60] Schwartzentruber, J. *et al.* Genome-wide meta-analysis, fine-mapping and integrative prioritization implicate new Alzheimer's disease risk genes. *Nature Genetics* **53**, 392–402 (2021).

[61] Anderson, M. J. A new method for non-parametric multivariate analysis of variance. *Austral Ecology* **26**, 32–46 (2001).

[62] Schapira, A. H. V. *et al.* Mitochondrial Complex I Deficiency in Parkinson's Disease. *Journal of Neurochemistry* **54**, 823–827 (1990).

[63] Bose, A. & Beal, M. F. Mitochondrial dysfunction in Parkinson's disease. *Journal of Neurochemistry* **139**, 216–231 (2016).

[64] Theodore, S., Cao, S., McLean, P. J. & Standaert, D. G. Targeted Overexpression of Human α-Synuclein Triggers Microglial Activation and an Adaptive Immune Response in a Mouse Model of Parkinson Disease. *Journal of Neuropathology & Experimental Neurology* **67**, 1149–1158 (2008).

[65] Zhou, X., Song, H., He, J., Han, W. & Li, Q. Deciphering microglial activation and neuronal apoptosis post-traumatic brain injury: The role of TYROBP in inflammation regulation networks. *Molecular Medicine Reports* **29**, 1–20 (2024).

[66] Stoll, A. C. *et al.* Neuroinflammatory gene expression profiles of reactive glia in the substantia nigra suggest a multidimensional immune response to alpha synuclein inclusions. *Neurobiology of Disease* **191**, 106411 (2024).

[67] Ki, S. M., Jeong, H. S. & Lee, J. E. Primary Cilia in Glial Cells: An Oasis in the Journey to Overcoming Neurodegenerative Diseases. *Frontiers in Neuroscience* **15** (2021).

[68] Bae, J.-E. *et al.* Primary cilia mediate mitochondrial stress responses to promote dopamine neuron survival in a Parkinson's disease model. *Cell Death & Disease* **10**, 952 (2019).

[69] Maïza, A. *et al.* The role of heparan sulfates in protein aggregation and their potential impact on neurodegeneration. *FEBS Letters* **592**, 3806–3818 (2018).

[70] Videira, P. A. Q. & Castro-Caldas, M. Linking Glycation and Glycosylation With Inflammation and Mitochondrial Dysfunction in Parkinson's Disease. *Frontiers in Neuroscience* **12** (2018).

[71] Wersinger, C., Jeannotte, A. & Sidhu, A. Attenuation of the norepinephrine transporter activity and trafficking via interactions with α-synuclein. *European Journal of Neuroscience* **24**, 3141–3152 (2006).

[72] Espay, A. J., LeWitt, P. A. & Kaufmann, H. Norepinephrine deficiency in Parkinson's disease: The case for noradrenergic enhancement. *Movement Disorders* **29**, 1710–1719 (2014).

[73] Seeker, L. A. *et al.* Brain matters: unveiling the distinct contributions of region, age, and sex to glia diversity and CNS function. *Acta Neuropathologica Communications* **11**, 84 (2023).

[74] Pandey, S. *et al.* Disease-associated oligodendrocyte responses across neurodegenerative diseases. *Cell Reports* **40**, 111189 (2022).

[75] Gijón, M. A., Riekhof, W. R., Zarini, S., Murphy, R. C. & Voelker, D. R. Lysophospholipid acyltransferases and arachidonate recycling in human neutrophils. *The Journal of Biological Chemistry* **283**, 30235–30245 (2008).

[76] Mi, S. *et al.* Death receptor 6 negatively regulates oligodendrocyte survival, maturation and myelination. *Nature Medicine* **17**, 816–821 (2011).

[77] Richter-Landsberg, C. The Cytoskeleton in Oligodendrocytes. *Journal of Molecular Neuroscience* **35**, 55–63 (2008).

[78] Williams, T. D. & Rousseau, A. Translation regulation in response to stress. *The Febs Journal* **291**, 5102–5122 (2024).

[79] Clayton, B. L. L. & Popko, B. Endoplasmic reticulum stress and the unfolded protein response in disorders of myelinating glia. *Brain Research* **1648**, 594–602 (2016).

[80] Chaari, A., Hoarau-Véchot, J. & Ladjimi, M. Applying chaperones to protein-misfolding disorders: Molecular chaperones against α-synuclein in Parkinson's disease. *International Journal of Biological Macromolecules* **60**, 196–205 (2013).

[81] Tepavčević, V. Oligodendroglial Energy Metabolism and (re)Myelination. *Life* **11**, 238 (2021).

[82] Kim, S.-H., Cho, Y.-S. & Jung, Y.-K. Failure of lysosomal acidification and endomembrane network in neurodegeneration. *Experimental & Molecular Medicine* **57**, 2418–2428 (2025).

[83] Wolf, F. A., Angerer, P. & Theis, F. J. SCANPY: large-scale single-cell gene expression data analysis. *Genome Biology* **19**, 15 (2018).

[84] Korsunsky, I. *et al.* Fast, sensitive and accurate integration of single-cell data with Harmony. *Nature Methods* **16**, 1289–1296 (2019).

[85] Traag, V. A., Waltman, L. & Van Eck, N. J. From Louvain to Leiden: guaranteeing well-connected communities. *Scientific Reports* **9**, 5233 (2019).

[86] McInnes, L., Healy, J. & Melville, J. UMAP: Uniform Manifold Approximation and Projection for Dimension Reduction (2020). URL http://arxiv.org/abs/1802.03426.

[87] Wolock, S. L., Lopez, R. & Klein, A. M. Scrublet: Computational Identification of Cell Doublets in Single-Cell Transcriptomic Data. *Cell Systems* **8**, 281–291.e9 (2019).

[88] Mathys, H. *et al.* Single-cell multiregion dissection of Alzheimer's disease. *Nature* **632**, 858–868 (2024).

[89] Daniel, S. F. *et al.* MapMyCells: High-performance mapping of unlabeled cell-by-gene data to reference brain taxonomies (2026). URL https://www.biorxiv.org/content/10.64898/2026.03.06.710160v1.

[90] Badia-i Mompel, P. *et al.* decoupleR: ensemble of computational methods to infer biological activities from omics data. *Bioinformatics Advances* **2**, vbac016 (2022).

[91] Chen, Y., Chen, L., Lun, A. L., Baldoni, P. & Smyth, G. edgeR v4: powerful differential analysis of sequencing data with expanded functionality and improved support for small counts and larger datasets. *Nucleic Acids Research* **53**, gkaf018 (2025).

[92] Heumos, L. *et al.* Pertpy: an end-to-end framework for perturbation analysis (2024). URL http://biorxiv.org/lookup/doi/10.1101/2024.08.04.606516.

[93] Ritchie, M. E. *et al.* limma powers differential expression analyses for RNA-sequencing and microarray studies. *Nucleic Acids Research* **43**, e47 (2015).

[94] Oksanen, J. *et al.* vegan: Community Ecology Package (2026). URL https://cran.r-project.org/web/packages/vegan/index.html.

[95] Yu, G. Thirteen years of clusterProfiler. *The Innovation* **5**, 100722 (2024).

[96] Dolgalev, I. msigdbr: MSigDB Gene Sets for Multiple Organisms in a Tidy Data Format (2025). URL https://igordot.github.io/msigdbr/.